

Precision and informational limits in inelastic optical spectroscopy

Peter Török^{1,2}, Matthew R. Foreman^{2*}

*School of Physical and Mathematical Sciences, Nanyang Technological University, Singapore and
Blackett Laboratory, Department of Physics, Imperial College London, Prince Consort Road, London, SW7 2AZ, UK*

(Dated: December 20, 2024)

Using Fisher information and the Cramér-Rao lower bound, we analyse fundamental precision limits in the determination of spectral parameters in inelastic optical scattering. General analytic formulae are derived which account for the instrument response functions of the dispersive element and relay optics found in practical Raman and Brillouin spectrometers. Limiting cases of dispersion and diffraction limited spectrometers, corresponding to measurement of Lorentzian and Voigt lineshapes respectively, are discussed in detail allowing optimal configurations to be identified. Effects of defocus, spherical aberration, detector pixellation and a finite detector size are also considered.

INTRODUCTION

Interactions between either acoustic or optical phonons in a material and an incident photon, can give rise to inelastic scattering, known more specifically as Brillouin or Raman scattering respectively [1, 2]. Such processes provide a means by which to probe the vibrational, micro-mechanical and compositional properties of samples [3–7]. As such, recent decades have seen development of a wealth of experimental techniques for acquisition of inelastic scattering spectra including fibre, imaging and near field based setups [8–13]. Inelastic scattering is, however, an intrinsically weak process. Despite improvements in achievable signal to noise ratios using surface enhancements, stimulated processes, interferometric or heterodyne detection [14–18], the value of experimental data can be dramatically degraded by noise. Systematic quantitative analysis of achievable precision in inelastic optical spectroscopy is, however, hitherto lacking and will thus form the focus of this article. Evaluation of such limits is not only of importance in terms of aiding system design [19–21], particularly in scenarios with limited photon budgets, but can also enable benchmarking of data processing algorithms and analysis protocols [22, 23].

Within this context, we first detail the model of signal acquisition adopted throughout this work. We restrict attention to measurement of spontaneous scattering spectra by means of angularly/spatially dispersive spectrometers, as opposed to scanning etalon based alternatives. In particular, our treatment incorporates the imperfect nature of the dispersive element required in any spectroscopic experiment, and allows for additional, potentially aberrated, relay optics. We then proceed to outline the information theoretic precision limit, given by the Cramér-Rao lower bound, as applied to the problem of extracting spectral parameters in inelastic spectroscopy. Finally, we apply these results to a number of limiting cases and numerical examples.

DETECTION MODEL IN SPECTROMETERS

An ideal spontaneous or thermally excited Brillouin or Raman spectrum consists of a central Rayleigh scattering peak flanked by the Stokes and anti-Stokes scattering peaks corresponding to generation or annihilation of a phonon. If the Rayleigh peak is centred at frequency ω_0 , then the two inelastic peaks are centred at $\omega_{\pm 1} = \omega_0 \pm \Omega$, where Ω is the inelastic frequency shift. Assuming each peak has an arbitrary lineshape $F(\omega, \omega_p, \Gamma_p)$ for $p = 0, \pm 1$, the associated complex amplitude of each spectral frequency component, denoted ω , is given by

$$s(\omega) = \sum_{p=-1}^{+1} A_p F(\omega; \omega_p, \Gamma_p) \quad (1)$$

where $\Gamma_{-1} = \Gamma_{+1} = \Gamma$ is the intrinsic FWHM of the inelastic peaks, Γ_0 is the intrinsic FWHM of the Rayleigh peak and $A_{\pm 1,0}$ describes their respective magnitudes. The lineshape is assumed to be normalised such that $\int_{-\infty}^{\infty} |F(\omega)|^2 d\omega = 1$, meaning that $|A_p|^2$ describes the total power in a given spectral peak. Assuming any measurements are made over a time long compared to the phonon coherence time and restricting attention to spontaneous inelastic processes it follows that the power spectrum is

$$S(\omega) = |s(\omega)|^2 = \sum_{p=-1}^{+1} |A_p|^2 |F(\omega; \omega_p, \Gamma_p)|^2. \quad (2)$$

In this work we will assume that the spectral lineshapes are Lorentzian in nature, i.e. $F(\omega, \omega_p, \Gamma_p) = L(\omega; \omega_p, \Gamma_p)$ where

$$L(\omega; \omega_p, \Gamma_p) = \sqrt{\frac{2}{\pi \Gamma_p}} \frac{i \Gamma_p / 2}{(\omega - \omega_p) + i \Gamma_p / 2}. \quad (3)$$

In an experimental scenario an observed spectrum is subject to the instrumental response of the spectrometer used to measure it [24, 25], such that the measured lineshape may not be a pure Lorentzian. The core function of an optical spectrometer is to spatially separate each individual frequency component, ω , present in an input

* matthew.foreman@imperial.ac.uk

wave. To achieve this a dispersive element, such as a grating or virtually imaged phase array (VIPA) [26], is used to discriminate different frequency components through the angle at which they are diffracted or transmitted. By placing a detector in the far field region of the dispersive element, the angular discrimination is converted to a spatial separation of differing frequency components through diffraction alone. In practice, the dispersive element produces a spatially extended distribution on the detector even for a monochromatic input as can be described by the associated complex amplitude response function $h_{\text{disp}}(x, \omega)$, where x describes the spatial coordinate in the detector plane. Note that since single or stand alone dispersive devices only produce a one-dimensional angular separation we restrict our discussion to a single spatial coordinate x . Nevertheless, our analysis applies to any number of dispersive spectrometers arranged in a crossed configuration along the direction of dispersion. High finesse VIPAs, for example, give rise to Lorentzian peaks on the detector for a monochromatic input. For simplicity, in this work we also assume a linear mapping between the input frequency of light and the ideal location of the resulting peak on the detector, such that

$$h_{\text{disp}}(x, \omega) = h_{\text{disp}}(x - x_0(\omega)) \quad (4)$$

where $x_0(\omega) = \alpha(\omega - \omega_{\text{off}})$, α describes the scaling constant between frequency and real space and ω_{off} allows for an arbitrary spectral offset. To account for the finite free spectral range (FSR), Ω_{FSR} , inherent in a spectrometer we let

$$h_{\text{disp}}(x - x_0) = \sum_{q=-\infty}^{\infty} B_q \bar{h}_{\text{disp}}(x - x_0 + \alpha q \Omega_{\text{FSR}}) \quad (5)$$

where the different FSRs are indexed by q and we have assumed that the lineshape of an individual peak, \bar{h}_{disp} , is the same for each FSR up to a slowly varying amplitude variation described by the factor B_q . We shall also make the further simplifying assumption that $\sum_{q=-\infty}^{\infty} |B_q|^2 = 1$, which assuming $\Omega_{\text{FSR}} \gg \gamma_{\text{disp}}$, where γ_{disp} parametrises the width of \bar{h}_{disp} , implies $\int_{-\infty}^{\infty} |h_{\text{disp}}|^2 dx = \int_{-\infty}^{\infty} |\bar{h}_{\text{disp}}|^2 dx$.

Although the angular dispersion of a dispersive element can be converted to a spatial separation by detection in the Fraunhofer zone as discussed above, more commonly additional optics are placed after the dispersive element since this enables smaller device footprints and greater ease of use. One simple means by which this transformation can be achieved is to place a single lens a focal length from the exit surface of the dispersive element so as to achieve a Fourier transform of the output waveform. Introduction of such optics, which are not ideal, degrades the final detected lineshape for a monochromatic input further. Non-ideality arises not only from the finite numerical aperture of practical optical elements, but also due to aberrations that may be present.

Whilst all lens aberrations modify the shape of the amplitude response function (also known as the point spread function or PSF), the resulting consequences can differ in the context of inelastic spectroscopy. Aberrations that change the location of the maximum of a peak on the detector, for example, can result in erroneous estimates of the absolute frequency of that peak if they are not properly accounted for. Tilt, for example, produces a uniform shift of all peaks which can give rise to a systematic frequency shift, although practically tilt is of little interest as it is easily removable via calibration. Field-dependent shifts, on the other hand, arising from say coma or distortion, not only can give rise to errors in the estimated spectral frequency but also consequently in the inferred Brillouin or Raman shifts. Aberrations that change the observed shape (but not position) of a peak uniformly throughout the detection field (i.e. defocus and spherical aberration) can instead lead to systematic errors in the determination of the peak width which is a measure of the phonon decay lifetime. Such errors, can however become non-systematic, if an aberration affects the peak width differently depending on field position (e.g. curvature of field).

In addition to their effect on the observed lineshape, strong aberrations can also produce a non-linear spatial dispersion. Minimisation of aberrations is however usually sought through appropriate optical design, such that we can reasonably restrict attention to the weakly aberrated regime. The spectral amplitude response function of the dispersive element and additional optics combined can in this case can be described by

$$h_{\text{spec}}(x, \omega) = h_{\text{disp}}(x - x_0(\omega)) \otimes h_{\text{opt}}(x, \omega), \quad (6)$$

where $h_{\text{opt}}(x, \omega)$ is the PSF of the relay optics and we have implicitly assumed that the response functions are shift invariant. Since the spectral bandwidths encountered in Brillouin spectroscopy are small we shall also assume that we can safely neglect chromatic aberrations such that $h_{\text{opt}}(x, \omega) = h_{\text{opt}}(x)$. Within the context of Raman spectroscopy in which larger bandwidths are encountered we assume that optics are corrected for chromatic aberration. Although introduced in relation to h_{disp} , the parameter α appearing in $x_0(\omega)$ is now also used to account for additional linear scale factors between ω and x that may arise from the relay optics.

The assumption of shift invariance made in Eq. (6) is a limitation to our theory, since it means only field-independent monochromatic aberrations, i.e. defocus and spherical aberration can be described. In order to gauge under what experimental conditions our results might therefore be applicable, we briefly digress to consider the Maréchal condition as applied to possible coma (the lowest order field dependent aberration) in the lens. The Maréchal condition [27] requires the Seidel sum for coma to be less than 1.2λ for the optical system to be diffraction limited. For a singlet lens, the focal length thus needs to satisfy $f^3 \geq (X^2 d^2)/(2.4\lambda)$ where d is the marginal ray height at the lens. Figure 1 shows the mini-

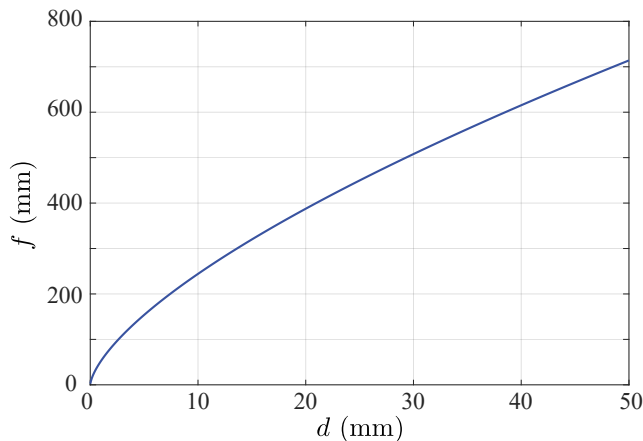


FIG. 1. Minimum focal length for which coma in a singlet lens can be safely neglected as determined using the Maréchal condition.

imum required focal length for a singlet assuming a detector size of $X = 14$ mm and a wavelength of $\lambda = 561$ nm. For more complex lenses, such as achromatic doublets, a simple analogous criterion does not exist meaning aberration tolerances of these lenses must instead be determined individually. As an example, assuming the same detector size as above, the Seidel sum of an achromatic doublet supplied by a popular optical component manufacturer of focal length $f = 100$ mm and diameter $2d = 50$ mm, is $S_{II} = 1.9\lambda$. Since coma is a linear function of field position, a maximum detector size that can hence be used with this lens is $X = 8.8$ mm, thus highlighting the need for careful analysis of aberrations before a lens can be safely used.

Returning now to our detection model, we note that the signal observed on a position resolving detector (initially neglecting pixellation) when a spectrum of frequencies is input is proportional to the total incident intensity. Assuming the detector integration time is long relative to the optical periods involved, the observed signal at a position x is hence

$$I_{\text{det}}(x) = N\Pi\left(\frac{x}{X}\right) \int_0^\infty S(\omega) |h_{\text{spec}}(x, \omega)|^2 d\omega \quad (7)$$

where $\Pi(z)$ is the top hat function defined by

$$\Pi(z) = \begin{cases} 0 & \text{for } |z| > 1/2 \\ 1 & \text{for } |z| < 1/2 \\ 1/2 & \text{for } |z| = 1/2 \end{cases}, \quad (8)$$

X is the full spatial width of the detector, and N is a normalisation constant which will be discussed later. Using Eq. (2) and Eqs. (5)–(7) we thus have

$$I_{\text{det}}(x) = N\Pi\left(\frac{x}{X}\right) \sum_{p,q} |A_p|^2 |B_q|^2 \int_0^\infty |L(\omega; \omega_p, \Gamma_p)|^2 \times \left| \int_{-\infty}^\infty \bar{h}_{\text{disp}}(x' - x_0(\omega)) h_{\text{opt}}(x' - x) dx' \right|^2 d\omega. \quad (9)$$

In this work we adopt simple models for the response function of the dispersive element and relay optics. Firstly we shall assume that the lineshape produced by the dispersive element is Lorentzian in profile such that

$$\bar{h}_{\text{disp}}(x) = AL(x, x_0, \gamma_{\text{disp}}) e^{i\kappa x}, \quad (10)$$

where A is a scale factor and we have allowed for a phase tilt for reasons that will become apparent below. The associated coherent transfer function of the dispersive element, defined as the Fourier transform of the amplitude response function, is hence given by the one sided exponential, viz.

$$\begin{aligned} \tilde{h}_{\text{disp}}(k_x) &= \frac{1}{2\pi} \int_{-\infty}^\infty h_{\text{disp}}(x) e^{-ik_x x} dk_x, \\ &= \exp\left[\left(-\frac{\gamma_{\text{disp}}}{2} + ix_0\right)(k_x - \kappa)\right] \Theta[k_x - \kappa], \end{aligned} \quad (11)$$

where k_x denotes the spatial frequency coordinate in the Fourier domain and the Heaviside function $\Theta[k_x - \kappa]$ is unity for $k_x \geq \kappa$ and zero otherwise. To ensure the dispersive element is passive ($|\tilde{h}_{\text{disp}}(k_x)| \leq 1$ for all k_x) the scale factor has been set to $A = [2\pi/\gamma_{\text{disp}}]^{1/2}$.

To model the PSF $h_{\text{opt}}(x)$ of the relay optics, we consider a single, potentially aberrated, lens of finite numerical aperture, NA, such that [28]

$$h_{\text{opt}}(x) = \int_{-\infty}^\infty \Pi\left[\frac{k_x}{k_0 \text{NA}}\right] \exp[iW(k_x)] e^{ik_x x} dk_x \quad (12)$$

where $\tilde{h}_{\text{opt}}(k_x) = \Pi[k_x/(k_0 \text{NA})] \exp[iW(k_x)]$ (defined analogously to Eq. (11)) is the coherent transfer function of the lens, $W(k_x)$ is a phase aberration represented as

$$W(k_x) = \sum_n a_n L_n(k_x) \quad (13)$$

and $L_n(k_x)$ is the n th order Legendre polynomial. Note that we use the Legendre polynomials to represent the perturbed wavefront since these are more appropriate for the one-dimensional problem [29]. In the presence of field dependent aberrations a_n is a function of observation position x , however, our assumption of shift invariance precludes this possibility such that we can only legitimately consider defocus ($n = 2$) and spherical aberration. Restricting to primary spherical aberration ($n = 4$) only we have $a_n = 0$ for $n \neq 2, 4$.

Finally we must define the normalisation constant N . Specifically, N is defined in terms of the total integrated intensity that would impinge on an infinite detector, $I_\infty = \lim_{X \rightarrow \infty} \int_{-\infty}^\infty I_{\text{det}}(x) dx$, such that

$$\begin{aligned} I_\infty &= N \sum_{p,q} |A_p|^2 |B_q|^2 \\ &\times \int_{-\infty}^\infty \int_0^\infty |L(\omega; \omega_p, \Gamma_p)|^2 |h_{\text{spec}}(x - x_0(\omega))|^2 d\omega dx. \end{aligned} \quad (14)$$

Upon reordering the integrals we find

$$N = \frac{I_\infty}{\sum_{p=-1}^{+1} |A_p|^2} \frac{1}{\int_{-\infty}^{\infty} |h_{\text{spec}}(x)|^2 dx}. \quad (15)$$

We can evaluate the integral factor in Eq. (15) using Parseval's theorem ultimately yielding

$$N = \frac{1}{2\pi} \frac{\gamma_{\text{disp}}}{1 - \exp[-(k_0 \text{NA} - \kappa)\gamma_{\text{disp}}]} \frac{I_\infty}{\sum_{p=-1}^{+1} |A_p|^2}. \quad (16)$$

Experimentally it is better to maximise the energy throughput of the spectrometer, which is limited due to the finite numerical aperture of the relay optics. Practically this implies that the field distribution at the exit surface of the dispersive element (corresponding to \tilde{h}_{disp}) is positioned so as to maximally fill the entrance pupil of the relay optics (described by the top hat function in \tilde{h}_{opt}). This corresponds, for the 1D case considered here, to selecting $\kappa = -k_0 \text{NA}$ yielding

$$N = \frac{1}{2\pi} \frac{\gamma_{\text{disp}}}{1 - \exp[-2k_0 \text{NA}\gamma_{\text{disp}}]} \frac{I_\infty}{\sum_{p=-1}^{+1} |A_p|^2}. \quad (17)$$

PARAMETRISING PRECISION WITH FISHER INFORMATION

Any experimental study is at heart an estimation problem, in which an observer estimates the value of some parameter(s) of interest from a noise corrupted signal. Ultimately we wish to consider the accuracy to which the inelastic shift Ω can be determined since this is the principle parameter of interest in inelastic spectroscopy. It is frequently reasonable to assume that the Rayleigh frequency ω_0 is known *a priori* since measurements are generally performed using a pre-calibrated laser excitation source. For completeness, however, we assume ω_0 is also unknown. Analysis of the precision limits can be simplified by considering the related problem of estimating the centre of mass frequency of the spectrum (determined from a single FSR) $\bar{\omega}$ and the separation of the two inelastic peaks $\bar{\Omega} = 2\Omega$, i.e. we consider estimation of the parameter vector $\mathbf{w} = (\bar{\omega}, \bar{\Omega})$. This alternative parameterisation is notably more suitable for cases in which the Rayleigh peak is saturated on the detector, or suppressed [18] which can hence hamper direct determination of ω_0 and Ω . The centre of mass of the spectrum is given by

$$\begin{aligned} \bar{\omega} &= \frac{\int_{-\infty}^{\infty} \omega S(\omega) d\omega}{\int_{-\infty}^{\infty} S(\omega) d\omega} \\ &= \omega_0 + \frac{(|A_{+1}|^2 - |A_{-1}|^2)\Omega}{|A_{-1}|^2 + |A_0|^2 + |A_{+1}|^2} \triangleq \omega_0 + \chi \frac{\bar{\Omega}}{2}. \end{aligned} \quad (18)$$

It hence follows that $\omega_{\pm 1} = \bar{\omega} - (\chi \mp 1)\bar{\Omega}/2$. Henceforth we assume that $x_0 = \alpha(\omega - \bar{\omega} + q\Omega_{\text{FSR}}) + \bar{x}$ such that the centre of mass of the spectrum is ideally located at \bar{x} .

In some applications, it may be of interest to estimate further spectral parameters (or indeed required by fitting algorithms), such as the width of each peak from which phonon lifetimes can be determined. For completeness in what follows we shall thus consider the expanded parameter vector $\mathbf{w} = (\bar{\omega}, \bar{\Omega}, \{\Gamma_p\}, \{|A_p|^2\})$, however in our numerical examples we shall principally restrict attention to the achievable precision when determining the inelastic frequency shift.

The parameter vector \mathbf{w} is not measured directly, but is instead inferred from noisy intensity measurements on the detector. In the previous section we neglected pixelation of the detector, however, in reality this is unreasonable and we thus relax this restriction now. In the ideal noise free case, the measured intensities from each pixel form a data vector $\mathbf{I}_{\text{det}} = [I_1, I_2, \dots, I_{N_p}]$ where N_p is the total number of pixels,

$$I_j = \int_{X_j} I_{\text{det}}(x) dx, \quad (19)$$

X_j is the domain of the j th pixel i.e. $x \in [x_j - \Delta/2, x_j + \Delta/2]$, Δ is the pixel size and x_j is the centre of the pixel. Accordingly the measured data vector takes the form $\mathbf{I}_{\text{meas}} = \mathbf{I}_{\text{det}} + \delta\mathbf{I}$ where $\delta\mathbf{I}$ is an unknown noise vector.

The expected precision of an observer's estimate of a parameter vector \mathbf{w} can be conveniently parametrised using the covariance matrix, $\mathbb{K}_{\mathbf{w}}$, derived from, for example, repeated measurements. The Cramér-Rao lower bound (CRLB), however, states that the covariance matrix $\mathbb{K}_{\mathbf{w}}$ for an ideal observer is lower bounded by the inverse of the so-called Fisher information matrix (FIM) $\mathbb{J}_{\mathbf{w}}$ according to the matrix inequality [30]

$$\mathbb{K}_{\mathbf{w}} \geq \mathbb{J}_{\mathbf{w}}^{-1}, \quad (20)$$

where the FIM is defined as

$$\mathbb{J}_{\mathbf{w}} = E \left[\left(\frac{\partial \ln f_{\mathbf{I}}(\mathbf{I}_{\text{meas}}|\mathbf{w})}{\partial \mathbf{w}} \right)^T \frac{\partial \ln f_{\mathbf{I}}(\mathbf{I}_{\text{meas}}|\mathbf{w})}{\partial \mathbf{w}} \right] \quad (21)$$

$$= E \left[\left(\frac{\partial}{\partial \mathbf{w}} \left[\frac{\partial}{\partial \mathbf{w}} \ln f_{\mathbf{I}}(\mathbf{I}_{\text{meas}}|\mathbf{w}) \right]^T \right)^T \right], \quad (22)$$

$f_{\mathbf{I}}(\mathbf{I}_{\text{meas}}|\mathbf{w})$ is the probability density function (PDF) describing the conditional probability of measuring a particular value of \mathbf{I}_{meas} for a given \mathbf{w} and $E[\dots]$ denotes the statistical expectation. The CRLB also implies the weaker set of inequalities $\sigma_{w_i}^2 \geq 1/[\mathbb{J}_{\mathbf{w}}]_{ii}$, where $\sigma_{w_i}^2$ is the estimation variance for each individual parameter w_i . It is important to note, however, that the CRLB as expressed by Eq. (20) explicitly quantifies the uncertainty achievable by *any* unbiased estimator and hence represents a fundamental limit to measurement precision, which can be asymptotically achieved using a maximum likelihood estimator [30].

Using the chain rule, the FIM can be expressed in the alternative form [31]

$$\mathbb{J}_{\mathbf{w}} = \left(\frac{\partial \mathbf{I}_{\text{det}}}{\partial \mathbf{w}} \right)^T \mathbb{J}_{\mathbf{I}_{\text{det}}} \left(\frac{\partial \mathbf{I}_{\text{det}}}{\partial \mathbf{w}} \right), \quad (23)$$

where $\mathbb{J}_{\mathbf{I}_{\text{det}}}$ is defined analogously to (22) in terms of the conditional PDF $f_{\mathbf{I}}(\mathbf{I}_{\text{meas}}|\mathbf{I}_{\text{det}})$. At this point we make the simplifying assumption that the noise on each pixel is statistically independent and identically distributed according to a Gaussian PDF, i.e.

$$f_{\mathbf{I}}(\mathbf{I}_{\text{meas}}|\mathbf{I}_{\text{det}}) = \frac{1}{\sqrt{2\pi\sigma^2}} \exp \left[-\frac{\mathbf{I}_{\text{det}} \cdot \mathbf{I}_{\text{det}}}{2\sigma^2} \right] \quad (24)$$

from which it follows that $\mathbb{J}_{\mathbf{I}_{\text{det}}} = \mathbb{I}/\sigma^2$ where \mathbb{I} is the $N_p \times N_p$ identity matrix. Hence

$$[\mathbb{J}_{\mathbf{w}}]_{kl} = \sum_j \frac{1}{\sigma^2} \frac{\partial I_j^I}{\partial w_k} \frac{\partial I_j^I}{\partial w_l}, \quad (25)$$

where w_k is the k th element of \mathbf{w} and $[\mathbb{J}_{\mathbf{w}}]_{kl}$ denotes the (j, k) th element of the FIM. The assumption of statistically independent and identically distributed noise implies that the dominant noise source is white in colour. Realistic noise sources, however, can frequently induce correlations between the noise for differing spectral components or on each pixel. Nevertheless, with knowledge of the power spectral density of the noise source a pre-whitening filter can be constructed and applied, as is common in signal processing applications [30]. Moreover, coloured noise can be more fully treated within the framework of asymptotic Fisher information as has been discussed in Refs. 32 and 33.

NUMERICAL EXAMPLES AND LIMITING CASES

Having established a theoretical framework to describe the obtainable precision in inelastic optical spectroscopy, we now consider a number of examples to illustrate the key experimental dependencies. Although the FIM can be evaluated numerically for the general case using Eqs. (9), (19) and (25), we can also obtain analytic results for a number of limiting cases. Numerical examples will be restricted to consideration of the precision in determining $\bar{\Omega}$, as parametrised by $J_{\bar{\Omega}, \bar{\Omega}} = J_{\Omega, \Omega}/4$ only, since determination of the frequency shift Ω from inelastic scattering of light is the core task of inelastic optical spectroscopy, however, we will derive analytic results for all elements of the FIM.

Infinite-extent finely-pixelated detector : dispersion limited

We first consider the case in which pixellation of the detector is fine with respect to the spatial widths of any

spectral features, i.e. $\Delta \ll \alpha\Gamma_p$, for $p = 0, \pm 1$. The detector is also assumed to be infinite in spatial extent. The lineshape of the detected spectrum is assumed to be dictated by the Lorentzian lineshape of the underlying inelastic and Rayleigh peaks and the response function of the dispersive element. Physically, this implies that the spatial width of the PSF, γ_{opt} , is also much smaller than the spatial widths of any spectral features and that of the grating or VIPA, denoted γ_{disp} , i.e. $\gamma_{\text{opt}} \ll \alpha\Gamma_p$ and $\gamma_{\text{opt}} \ll \gamma_{\text{disp}}$. With these assumptions we can make the approximations $\bar{h}_{\text{disp}}(x - x_0) = L(x'; \alpha(\omega - \bar{\omega} + q\Omega_{\text{FSR}}) + \bar{x}, \gamma_{\text{disp}})$, $h_{\text{opt}}(x) = \delta(x)$ whereby from Eq. (9)

$$I_{\text{det}}^I(x) \approx N_I \sum_{p,q} |A_p B_q|^2 \int_0^\infty |L(\omega; \omega_0 + p\Omega, \Gamma_p)|^2 \times |L(x, \bar{x} + \alpha(\omega - \bar{\omega} + q\Omega_{\text{FSR}}), \gamma_{\text{disp}})|^2 d\omega. \quad (26)$$

Note that here we use the normalisation constant N_I (in distinction to N used for the general case above) since we have applied an arbitrary scaling to \bar{h}_{disp} and $h_{\text{opt}}(x)$ for mathematical convenience. Specifically, we have $N_I = I_\infty / \sum_{p=-1}^+ |A_p|^2$. Noting $L(z - a; z_p, \zeta_p) = L(z, z_p + a, \zeta_p)$ and $L(z/a; z_p/a, \zeta_p/a) = \sqrt{a}L(z; z_p, \zeta_p)$ (as follow from inspection of Eq. (3)), Eq. (26) can be transformed to

$$I_{\text{det}}^I(x) \approx N_I \sum_{p,q} |A_p B_q|^2 \int_{-\infty}^\infty |L(\alpha\omega; \alpha(\omega_0 + p\Omega), \alpha\Gamma_p)|^2 \times |L(x - \alpha\omega; \bar{x} + \alpha(q\Omega_{\text{FSR}} - \bar{\omega}), \gamma_{\text{disp}})|^2 d(\alpha\omega), \quad (27)$$

where we have also assumed that we are considering frequencies which are large compared to the relevant linewidths and spectral separations, such that we can safely extend the integration over ω to $-\infty$. Eq. (27) therefore shows that $I_{\text{det}}^I(x)$ is given by the convolution of two Lorentzians, which is itself a Lorentzian function. Specifically we find

$$I_{\text{det}}^I(x) \approx N_I \sum_{p,q} |A_p B_q|^2 |L(x; \bar{x} + \alpha\Omega_{pq}, \alpha\Gamma_p + \gamma_{\text{disp}})|^2 \quad (28)$$

where $\Omega_{pq} = (p - \chi)\bar{\Omega}/2 + q\Omega_{\text{FSR}}$. Now using Eq. (23) we can express the elements of the FIM as

$$[\mathbb{J}_{\mathbf{w}}]_{kl} \approx \frac{1}{\sigma^2 \Delta} \int_{-\infty}^\infty \frac{\partial I_j^I(x_j)}{\partial w_k} \frac{\partial I_j^I(x_j)}{\partial w_l} dx_j \quad (29)$$

where the integration range on x_j follows since we have assumed an infinite detector,

$$I_j^I = N_I \sum_{p,q} |A_p B_q|^2 \int_{X_j} |L[x; \bar{x} + \alpha\Omega_{pq}, \alpha\Gamma_p]|^2 dx \quad (30) \\ \approx N_I \sum_{p,q} |A_p B_q|^2 \Delta |L[x_j; \bar{x} + \alpha\Omega_{pq}, \alpha\Gamma_p]|^2 \quad (31)$$

and the approximations hold in the fine pixellation limit. Evaluating the derivatives in Eq. (29) (remembering that

$\bar{x} = \alpha(\bar{\omega} - \omega_{\text{off}})$ where ω_{off} is a pre-calibrated constant) we find

$$\frac{\partial I_j^I}{\partial \bar{\omega}} \approx N_I \Delta \sum_{p,q} |A_p B_q|^2 \frac{\alpha}{\pi} \frac{\gamma_p (x_j - \bar{x} - \alpha \Omega_{pq})}{[(x_j - \bar{x} - \alpha \Omega_{pq})^2 + \gamma_p^2/4]^2}, \quad (32)$$

$$\frac{\partial I_j^I}{\partial \Omega} \approx N_I \Delta \sum_{p,q} |A_p B_q|^2 \frac{\alpha}{2\pi} \frac{\gamma_p (p - \chi) (x_j - \bar{x} - \alpha \Omega_{pq})}{[(x_j - \bar{x} - \alpha \Omega_{pq})^2 + \gamma_p^2/4]^2}, \quad (33)$$

$$\frac{\partial I_j^I}{\partial \Gamma_p} \approx N_I \Delta \sum_q |A_p B_q|^2 \frac{\alpha}{2\pi} \frac{(x_j - \bar{x} - \alpha \Omega_{pq})^2 - \gamma_p^2/4}{[(x_j - \bar{x} - \alpha \Omega_{pq})^2 + \gamma_p^2/4]^2}, \quad (34)$$

$$\frac{\partial I_j^I}{\partial |A_p|^2} \approx N_I \Delta \sum_q \frac{|B_q|^2}{\pi} \frac{\gamma_p/2}{(x_j - \bar{x} - \alpha \Omega_{pq})^2 + \gamma_p^2/4}, \quad (35)$$

where $\gamma_p = \alpha \Gamma_p + \gamma_{\text{disp}}$. The form of the denominators in Eqs. (32)–(35) means that for a specific peak of order (p, q) the derivative term is only non-negligible in the region of the peak. As such when evaluating the product of derivative terms in Eq. (29) when $\Omega > \Gamma_0 + \Gamma$ (i.e. the inelastic and Rayleigh peaks are well separated) it is reasonable to neglect any cross terms between peaks of different orders. With this approximation, substitution of Eqs. (32)–(35) into Eq. (29) allows the integration to be performed, yielding

$$J_{\bar{\omega}, \bar{\omega}}^I = J_0 \sum_{p=-1}^{+1} \frac{2\alpha^2 |A_p|^4}{\pi(\alpha \Gamma_p + \gamma_{\text{disp}})^3}, \quad (36)$$

$$J_{\Omega, \Omega}^I = J_0 \sum_{p=-1}^{+1} \frac{\alpha^2 (p - \chi)^2 |A_p|^4}{2\pi(\alpha \Gamma_p + \gamma_{\text{disp}})^3}, \quad (37)$$

$$J_{\Gamma_p, \Gamma_{p'}}^I = \delta_{pp'} \sum_{p''=-1}^{+1} \delta_{|p||p''|} J_0 \frac{\alpha^2 |A_{p''}|^4}{2\pi(\alpha \Gamma_{p''} + \gamma_{\text{disp}})^3}, \quad (38)$$

$$J_{|A_p|^2, |A_{p'}|^2}^I = \delta_{pp'} \frac{J_0}{\pi(\alpha \Gamma_p + \gamma_{\text{disp}})} \quad (39)$$

$$J_{\bar{\omega}, \Omega}^I = J_0 \sum_{p=-1}^{+1} \frac{(p - \chi) \alpha^2 |A_p|^4}{\pi(\alpha \Gamma_p + \gamma_{\text{disp}})^3}, \quad (40)$$

$$J_{|A_p|^2, \Gamma_{p'}}^I = -\delta_{pp'} J_0 \frac{\alpha |A_p|^2}{2\pi(\alpha \Gamma_p + \gamma_{\text{disp}})^2}, \quad (41)$$

where $J_0 = N_I^2 \Delta \sum_{q=-\infty}^{\infty} |B_q|^4 / \sigma^2$. All other elements of the Fisher information matrix are zero, i.e. $J_{\bar{\omega}, \Gamma_p}^I = J_{\Omega, \Gamma_p}^I = J_{\bar{\omega}, |A_p|^2}^I = J_{\Omega, |A_p|^2}^I = 0$.

For many applications, the inelastic frequency shift Ω (or equivalently $\bar{\Omega}$) is the primary parameter of interest. In Brillouin spectroscopy, for example, the Brillouin shift is proportional to the acoustic velocity of phonons in a material and can thus provide insights into mechanical properties of a sample [10, 11]. The precision to which $\bar{\Omega}$ can be determined is parameterised by $J_{\bar{\Omega}, \bar{\Omega}}^I$. An example calculation of $J_{\bar{\Omega}, \bar{\Omega}}^I$ is therefore shown in Figure 2.

| Parameter | Symbol | Value |
|---------------------------------------|-----------------------|----------|
| Size of CCD | X | 14 mm |
| Free spectral range | Ω_{FSR} | 40 GHz |
| Relative amplitude of Rayleigh peak | A_0 | 1 |
| Relative amplitude of inelastic peaks | $A_{\pm 1}$ | 0.2 |
| Spectral width of Rayleigh peak | Γ_0 | 0.2 GHz |
| Spectral width of inelastic peaks | Γ | 0.2 GHz |
| Frequency shift | Ω | 12.5 GHz |
| Rayleigh wavelength | λ | 561 nm |

TABLE I. Values of simulations parameters common to all examples.

Curves shown are for a full numerical calculation (solid blue) using Eqs. (9), (19) and (25) and for the approximate analytic result (dashed gray) given in Eq. (37). For the numerical calculation the detector was necessarily finite in size and a relatively large numerical aperture of $\text{NA} = 0.2$ was used such that the PSF had a width of $\gamma_{\text{airy}} = 1.4 \mu\text{m}$ (or half a pixel), whereas the width of the dispersive element response function was set at 3 pixels ($8.4 \mu\text{m}$). Derivatives were calculated using a finite difference approximation. For simplicity only a single FSR was considered, i.e. $B_q = \delta_{q0}$ however it should be noted that this does not greatly affect our conclusions. All other simulation parameters are listed in Table I,

The Fisher information in Figure 2 is plotted as a

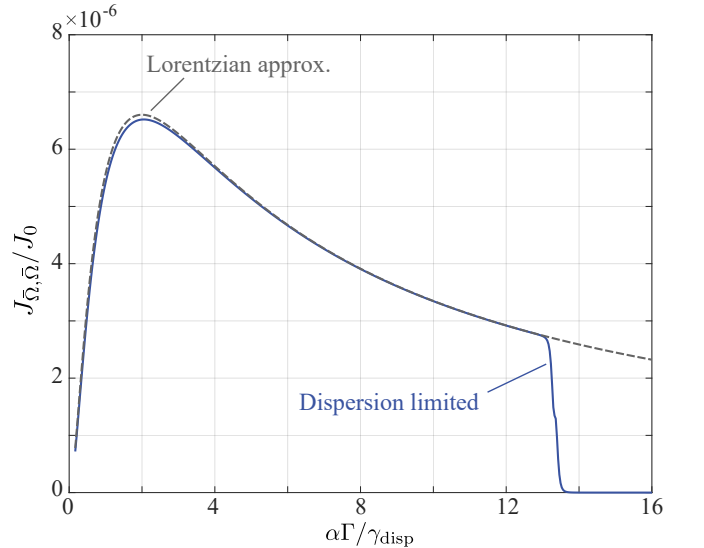


FIG. 2. Numerical calculation (blue solid line) of $J_{\bar{\Omega}, \bar{\Omega}}^I$ and the corresponding Lorentzian based approximation (dashed grey line). A finely pixellated detector with $N_p = 5000$ pixels was assumed. The width of the response function of the dispersive element was taken as $\gamma_{\text{disp}} = 8.4 \mu\text{m}$ and the relay lens assumed to have a numerical aperture of $\text{NA} = 0.2$ such that the spectrometer is dispersion limited. See Table I for other simulation parameters.

function of the ratio of the dimensionless parameter $\rho = \alpha\Gamma/\gamma_{\text{disp}}$ which describes the ratio of the intrinsic spatial width relative to the width of the dispersive element's response function. Good agreement between the numerical and approximate results is generally evident, except that the FI calculated numerically drops to zero at $\alpha\Gamma/\gamma_{\text{disp}} \sim 13$. This discrepancy will be discussed further below and arises because our numerical calculations necessarily consider a finite sized detector in contrast to the assumption made in our theoretical analysis.

Physical insight into the behaviour shown in Figure 2 and indeed into Eqs. (36)–(41) can be gained by first considering the case of a purely monochromatic input, but allowing for the finite width of the amplitude response function of the dispersive element ($\Gamma_p = 0$, $\gamma_{\text{disp}} \neq 0$). In this case the contribution to Eqs. (36)–(41) from each spectral peak follows an inverse power law (of varying degree) in the instrumental peak width γ_{disp} . As the spatial width of a peak decreases, so the energy contained within that peak is confined to a smaller area, such that the signal to noise ratio at each position on the detector improves and a better estimation precision ultimately results. In each non-zero element of the FIM, there is however an additional dependence on the scale factor α appearing in the numerator (with the exception Eq. (39)). This factor captures the intuitive expectation that spatial positions, separations or widths can be more precisely determined when they are magnified. Taking the estimation of $\bar{\Omega}$ as an illustrative example, we note that as α decreases so the inelastic peaks are positioned closer together on the detector, however, the finite (fixed) peak width means it is consequently harder to individually resolve the peaks and hence determine their separation.

Similarly, when considering an ideal spectrometer, but allowing for a finite intrinsic spectral width ($\gamma_{\text{disp}} = 0$, $\Gamma_p \neq 0$), we find that the non zero elements of the FI decrease as the spatial width, $\alpha\Gamma_p$, of the observed peaks increases. In this case however, since the intrinsic spatial width decreases with α , the difficulty in resolving individual peaks is somewhat mitigated. In the general dispersion limited case ($\gamma_{\text{disp}} \neq 0$, $\Gamma_p \neq 0$) the total observed linewidth is dictated by both the intrinsic spectral width and the broadening caused by the dispersive element, as reflected by the aggregate width $\alpha\Gamma_p + \gamma_{\text{disp}}$ appearing in the denominators of Eqs. (36)–(41), however the principles dictating the estimation precision are the same. Finally we note that whilst Eqs. (36)–(41) predict that the obtainable FI tends to infinity as $\alpha\Gamma_p + \gamma_{\text{disp}} \rightarrow 0$, this information divergence is of no physical relevance since the widths of the peaks on the detector become comparable to the pixel size in this limit hence invalidating our assumption of a finely pixellated detector. This case is considered in greater detail below.

The relative magnitude of α and γ_{disp} can be experimentally controlled, for example, by varying the magnification factor of the relay lens, so as to achieve an optimal balance between the two competing effects hence yielding

a maximum FI (or equivalent the best obtainable precision). When considering inelastic peaks of equal amplitude A Eq. (37), for example, can be written in the form

$$J_{\bar{\Omega}, \bar{\Omega}}^I = \frac{J_0 |A|^4}{\pi \gamma_{\text{disp}} \Gamma_{\pm 1}^2} \frac{\rho^2}{(1 + \rho)^3} \quad (42)$$

such that a maximum FI of $4J_0 |A|^4 / (27\pi \gamma_{\text{disp}} \Gamma_{\pm 1}^2)$ can be obtained when $\rho = 2$, or equivalently when the intrinsic spatial inelastic peak width is twice that of the amplitude response function of the dispersive element $\alpha\Gamma = 2\gamma_{\text{disp}}$. Similar maxima are also found in $J_{\bar{\omega}, \bar{\omega}}$ and $J_{\Gamma_p, \Gamma_{p'}}$, whereas the maximum correlation between estimates of $|A_p|^2$ and Γ_p (as described by $J_{|A_p|^2, \Gamma_p}$) occurs when $\rho = 1$ or equivalently $\alpha\Gamma = \gamma_{\text{disp}}$. There exists no optimal configuration for the remaining elements of the FIM.

Infinite-extent finely-pixellated detector : diffraction limited

In a similar vein to above we can determine the FIM for an infinite-extent, finely pixellated detector, however, instead of assuming the intensity distribution on the detector is limited by the response function of the dispersive element, we can instead consider the case in which the PSF, $h_{\text{opt}}(x)$, of the relaying optics dominates. For a one-dimensional case without aberrations, the finite numerical aperture NA of the optics implies that $h_{\text{opt}}(x) \sim \text{sinc}(\pi x / \gamma_{\text{Abbe}})$ where $\gamma_{\text{Abbe}} = \lambda / (2\text{NA})$ determines the position of the first zero of $h(x)$. For simplicity, however, we approximate the instrument response function by a Gaussian distribution,

$$G(x; x_p, \gamma_{\text{opt}}) = \frac{1}{(2\pi\gamma_{\text{opt}}^2)^{1/4}} \exp\left[-\frac{(x - x_p)^2}{4\gamma_{\text{opt}}^2}\right], \quad (43)$$

with a spatial width of γ_{opt} chosen so as to match the full-width half-maximum of the sinc function, implying $\gamma_{\text{opt}} = 1.89549\gamma_{\text{Abbe}} / (2\pi\sqrt{\ln 2}) = 0.36235\gamma_{\text{Abbe}}$. For this case we thus make the approximations: $\bar{h}_{\text{disp}}(x' - x_0) = \delta(x' - \alpha(\omega - \bar{\omega} + q\Omega_{\text{FSR}}) - \bar{x})$ and $h_{\text{opt}}(x) = G(x; 0, \gamma_{\text{opt}})$, whereby

$$I_{\text{det}}^{II}(x) = N_{II} \sum_{p,q} |A_p B_q|^2 \int_0^\infty |L(\omega; \omega_0 + p\Omega, \Gamma_p)|^2 \times |G(\alpha(\omega - \bar{\omega} + q\Omega_{\text{FSR}}) + \bar{x} - x; 0, \gamma_{\text{opt}})|^2 d\omega. \quad (44)$$

Again we use the normalisation constant N_{II} since we have scaled \bar{h}_{disp} and $h_{\text{opt}}(x)$ for convenience where we find $N_{II} = N_I$.

Once more using the properties of Lorentzians as above in addition to similar properties for Gaussian lineshapes we can write the resulting intensity distribution as the convolution of a Lorentzian and a Gaussian lineshape, i.e.

$$I_{\text{det}}^{II}(x) = N_{II} \sum_{p,q} |A_p B_q|^2 V(x; \bar{x} + \alpha\Omega_{pq}, \alpha\Gamma_p, \gamma_{\text{opt}}) \quad (45)$$

where $V(x; \bar{x} + \alpha\Omega_{pq}, \alpha\Gamma_p, \gamma_{\text{opt}})$ is the Voigt profile [34]. For simplicity we do not consider the full integral form for the Voigt profile, but instead restrict attention to the pseudo-Voigt distribution described in [34] whereby

$$V(x; \bar{x} + \alpha\Omega_{pq}, \alpha\Gamma_p, \gamma) \approx \eta_p |L(x; \bar{x} + \alpha\Omega_{pq}, \beta_p/\alpha)|^2 + (1 - \eta_p) |G(x; \bar{x} + \alpha\Omega_{pq}, \beta_p/(2\sqrt{2\ln 2}))|^2 \quad (46)$$

where $\mu_p = \beta_{L,p}/\beta_p$,

$$\eta_p = 1.36603\mu_p - 0.47719\mu_p^2 + 0.11116\mu_p^3, \quad (47)$$

$$\beta_p = [\beta_G^5 + 2.69269\beta_G^4\beta_{L,p} + 2.42843\beta_G^3\beta_{L,p}^2 + 4.47163\beta_G^2\beta_{L,p}^3 + 0.07842\beta_G\beta_{L,p}^4 + \beta_{L,p}^5]^{1/5} \quad (48)$$

and the full-width half-maximum (FWHM) of the Lorentzian and Gaussian intensity distributions are $\beta_{L,p} = 2\alpha\Gamma_p$ and $\beta_G = 2\sqrt{2\ln 2}\gamma_{\text{opt}}$ respectively. Using this approximation we rewrite $I_j = \sum_{p,q} \eta_p I_{pq}^L(x_j) + (1 - \eta_p) I_{pq}^G(x_j)$ where $I_{pq}^L(x_j)$ and $I_{pq}^G(x_j)$ derive from the Lorentzian and Gaussian terms of the (p, q) th order peak. Again neglecting any cross term between adjacent peaks and also neglecting any parameter dependence of η we have that

$$\frac{\partial I_j^{II}}{\partial w_k} \frac{\partial I_j^{II}}{\partial w_l} \approx \eta_p^2 \frac{\partial I_{pq}^L}{\partial w_k} \frac{\partial I_{pq}^L}{\partial w_l} + (1 - \eta_p)^2 \frac{\partial I_{pq}^G}{\partial w_k} \frac{\partial I_{pq}^G}{\partial w_l} + \eta_p(1 - \eta_p) \left[\frac{\partial I_{pq}^G}{\partial w_k} \frac{\partial I_{pq}^L}{\partial w_l} + \frac{\partial I_{pq}^L}{\partial w_k} \frac{\partial I_{pq}^G}{\partial w_l} \right], \quad (49)$$

where the dependence of I_{pq}^{\dots} on x_j has been suppressed for clarity. It then follows that the FIM can be partitioned into three contributions viz. $\mathbb{J}_{\mathbf{w}}^{II} = \mathbb{J}_{\mathbf{w}}^L + \mathbb{J}_{\mathbf{w}}^G + \mathbb{J}_{\mathbf{w}}^{GL}$. The first term, $\mathbb{J}_{\mathbf{w}}^L$, will take the same form as Eqs. (36)–(41) with the replacement $\gamma_{\text{disp}} \rightarrow 0$ and with an additional factor of η_p^2 within the summations. The FIM associated with the second term can be evaluated by following the same logic as in the previous section ultimately yielding

$$J_{\bar{\omega}, \bar{\omega}}^G = J_0 \sum_{p=-1}^{+1} (1 - \eta_p)^2 \frac{\alpha^2 |A_p|^4}{4\sqrt{\pi}\gamma_{\text{opt}}^3}, \quad (50)$$

$$J_{\bar{\Omega}, \bar{\Omega}}^G = J_0 \sum_{p=-1}^{+1} (1 - \eta_p)^2 \frac{\alpha^2 (p - \chi)^2 |A_p|^4}{16\sqrt{\pi}\gamma_{\text{opt}}^3}, \quad (51)$$

$$J_{|A_p|^2, |A_{p'}|^2}^G = \delta_{pp'} J_0 (1 - \eta_p)^2 \frac{\alpha^2}{2\sqrt{\pi}\gamma_{\text{opt}}}, \quad (52)$$

$$J_{\bar{\omega}, \bar{\Omega}}^G = J_0 \sum_{p=-1}^{+1} (1 - \eta_p)^2 \frac{\alpha^2 (p - \chi) |A_p|^4}{8\sqrt{\pi}\gamma_{\text{opt}}^3} \quad (53)$$

and $J_{\Gamma_p, \Gamma_{p'}}^G = J_{|A_p|^2, |A_{p'}|^2}^G = J_{\bar{\omega}, \Gamma_p}^G = J_{\bar{\Omega}, \Gamma_p}^G = J_{\bar{\omega}, |A_p|^2}^G = J_{\bar{\Omega}, |A_p|^2}^G = 0$. The cross FIM terms follow similarly and

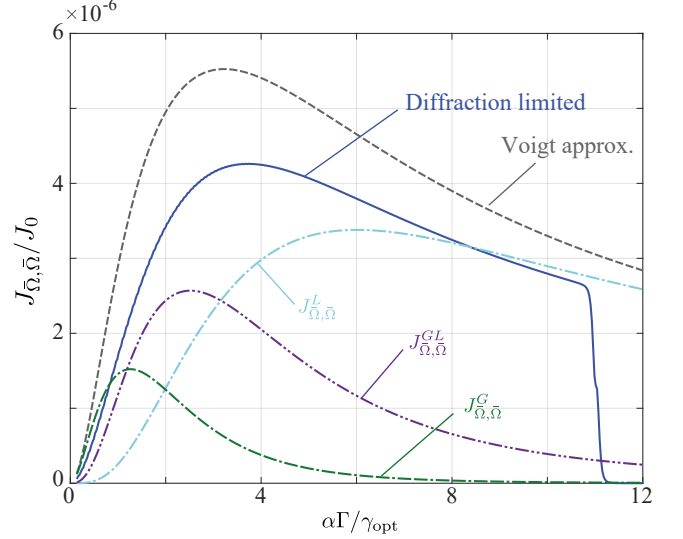


FIG. 3. Numerical calculation (blue solid line) of $J_{\bar{\Omega}, \bar{\Omega}}$ and the corresponding Voigt based approximation (dashed grey line). A finely pixellated detector with $N_p = 5000$ pixels was assumed. The width of the response function of the dispersive element was taken as $\gamma_{\text{disp}} = 8.4$ nm and the relay lens assumed to have a numerical aperture of $\text{NA} = 0.01$ such that the spectrometer is diffraction limited. See Table I for other simulation parameters. Individual contributions to the Voigt approximation are shown by the dot-dashed light blue, green and purple lines corresponding to Eqs. (37) (see also text), (51) and (55) respectively.

are given by

$$J_{\bar{\omega}, \bar{\omega}}^{GL} = J_0 \sum_{p=-1}^{+1} \eta_p (1 - \eta_p) |A_p|^4 \frac{\sqrt{2}\alpha^2}{\pi\gamma_{\text{opt}}^3} f(r_p), \quad (54)$$

$$J_{\bar{\Omega}, \bar{\Omega}}^{GL} = J_0 \sum_{p=-1}^{+1} \eta_p (1 - \eta_p) |A_p|^4 \frac{\alpha^2 (p - \chi)^2}{2\sqrt{2}\pi\gamma_{\text{opt}}^3} f(r_p), \quad (55)$$

$$J_{\bar{\omega}, \bar{\Omega}}^{GL} = J_0 \sum_{p=-1}^{+1} \eta_p (1 - \eta_p) |A_p|^4 \frac{(p - \chi)\alpha^2}{\sqrt{2}\pi\gamma_{\text{opt}}^3} f(r_p), \quad (56)$$

$$J_{|A_p|^2, |A_{p'}|^2}^{GL} = \delta_{pp'} J_0 \eta_p (1 - \eta_p) |A_p|^2 \frac{\alpha}{2\pi\gamma_{\text{opt}}^2} g(r_p), \quad (57)$$

$$J_{\bar{\omega}, |A_p|^2}^{GL} = \delta_{pp'} J_0 \eta_p (1 - \eta_p) \sqrt{\frac{2}{\pi}} \frac{w(r_p)}{\gamma_{\text{opt}}}, \quad (58)$$

where $r_p = \alpha\Gamma_p/(2\sqrt{2}\gamma_{\text{opt}})$,

$$f(z) = \sqrt{\pi} (2z^2 + 1) w(z) - 2z, \quad (59)$$

$$g(z) = \sqrt{\pi} z w(z) - 1, \quad (60)$$

$$w(z) = \exp[z^2] \text{erfc}[z] \quad (61)$$

and all other elements of $\mathbb{J}_{\mathbf{w}}^{GL}$ are zero.

Numerical results comparing the calculated FI $J_{\bar{\Omega}, \bar{\Omega}}$ to the analytic Voigt based approximation for the diffraction limited case are shown in Figure 3, now plotted as

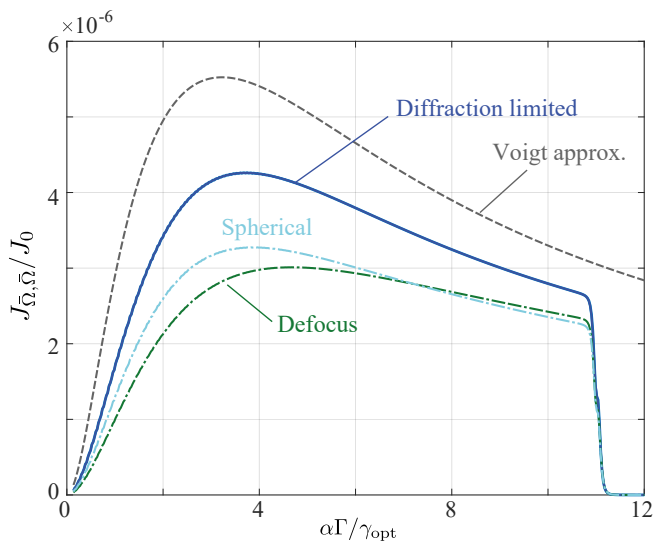


FIG. 4. Numerical results (blue solid curve) for the diffraction limited case (as per. Figure 3), with the addition of one wave of defocus (green dash-dotted curve) and spherical aberration (light blue dash-dotted curve). The Voigt based approximation is also shown by the grey dashed curve.

a function of the ratio $\tau = \alpha\Gamma/\gamma_{opt}$. Simulation parameters are again given in Table I. Additionally a numerical aperture of $NA = 0.01$ corresponding to $\gamma_{opt} \approx 3.6$ pixels was used, whilst a negligible value of $\gamma_{disp} = 8.4$ nm was assumed. Individual contributions to the analytic result from \mathbb{J}^L , \mathbb{J}^G and \mathbb{J}^{GL} are also shown. Good qualitative agreement between the numerical and approximate results are seen, however, for small τ numerical discrepancies are relatively large. This discrepancy is a result of the Gaussian approximation used to represent the PSF, with the exact functional form playing a more critical result in this regime (as reflected by the relative importance of \mathbb{J}^G and \mathbb{J}^{GL}). Aberrations present in the relay optics which alter the shape of the PSF (i.e. excluding tilt and piston) would thus be expected to have a significant effect at small τ (e.g. from use of larger magnifications), as is indeed borne out in calculations as shown in Figure 4. Specifically, we have plotted the variation of $J_{\bar{\Omega}, \bar{\Omega}}$ using the same parameters used for Figure 3, however, with the addition of one wave of defocus or spherical aberration. For each case the reduction in the obtainable FI, resulting from the overall PSF broadening, is similar in each case, however, the shift in the optimal τ is relatively small.

Figure 5 shows the numerical variation of $J_{\bar{\Omega}, \bar{\Omega}}$ for arbitrary values of γ_{disp} and γ_{opt} in the aberration free case, whereby it is seen that the obtainable precision monotonically decreases for fixed α as either response function broadens.

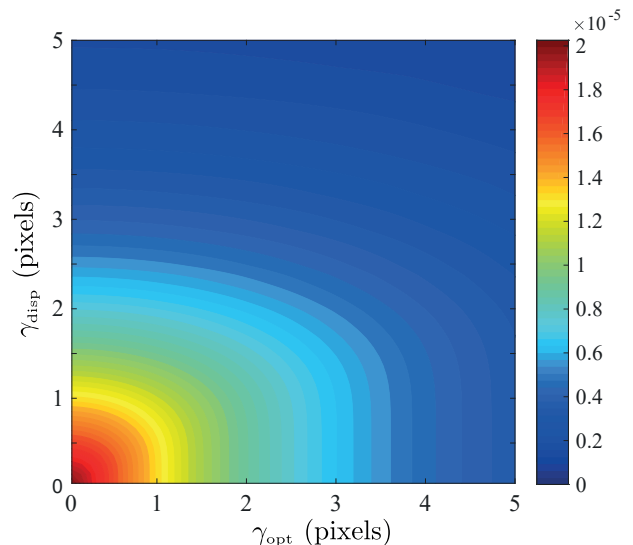


FIG. 5. Variation of $J_{\bar{\Omega}, \bar{\Omega}}$ as a function of the width of the PSF and dispersive element response function γ_{opt} and γ_{disp} assuming $\alpha\Omega_{FSR}/X = 0.25$.

Finite-extent finely-pixelated detector

The cases considered hitherto have assumed an infinite detector. Accordingly, when determining the elements of the FIM, the summation over each data point I_j (defined by Eq. (19)) could be accurately modelled by an integration over an infinite domain, as was done in Eq. (29). Upon considering the more realistic case of a detector of finite spatial extent X (albeit still finely pixelated), the integration domain in Eq. (29) must be restricted to X . Assuming that any given spectral feature does not straddle the edge of the detector, the effect of the finite integration domain is to limit the summation over q (and potentially p). Specifically, denoting the spatial position of the spectral peak indexed by p and q as $x_{pq} = \bar{x} + \alpha\Omega_{pq}$ and its associated experimental width by γ , the summations appearing in Eqs. (36)–(41) and (50)–(58) are only over peaks for which $\max[|x_{pq} \pm \gamma|] \lesssim X/2$. No information is obtained from peaks falling beyond the spatial extent of the detector as would be expected by intuition thus accounting for the drop in the calculated FI to zero seen in Figures 2–4. Only partial information is obtained for peaks which straddle the edge of the detector. Moreover, only a single FSR was considered in our discussion thus far, however, when multiple FSRs are present, a staggered fall off in the FI to zero is seen, with each step occurring when a single peak moves out of the detection area.

Coarse pixellation

To illustrate the effect of pixellation on the obtainable estimation accuracy it is sufficient to consider the FIM obtained from measurement of a single peak of the intensity distribution falling on the detector. We assume that the detector has N_p pixels indexed by $j = 1, 2, \dots, N_p$. Due to our assumption that each peak does not overlap significantly, the total FIM then follows by summing the information obtained for each individual peak (c.f. for example Eqs. (36)–(41)). For simplicity we shall assume a Lorentzian lineshape of width γ , such that

$$I_{\text{det}}(x) = |A_p|^2 |L(x; \bar{x} + \alpha(p - \chi)\Omega, \gamma)|^2. \quad (62)$$

In the extreme case of coarse pixellation we can assume that the pixels are so large that a single spectral peak spans only three pixels before falling to negligible intensities. The measured data values I_j are thus zero unless $n - 1 \leq j \leq n + 1$, where n is the index of the centre pixel of the three under consideration. Since we have assumed that $I_{\text{det}}(x) \approx 0$ on all but three pixels we can extend the integration domains appearing in Eq. (19), such that

$$I_j = \delta_{j,n-1} \int_{-\infty}^{x_n - \Delta/2} I_{\text{det}}(x) dx + \delta_{j,n} \int_{x_n - \Delta/2}^{x_n + \Delta/2} I_{\text{det}}(x) dx + \delta_{j,n+1} \int_{x_n + \Delta/2}^{\infty} I_{\text{det}}(x) dx. \quad (63)$$

For the Lorentzian lineshape assumed, the integration can be performed analytically yielding

$$I_{n \pm 1} = \frac{|A_p|^2}{\pi} \left[\frac{\pi}{2} \pm \arctan \left(\frac{x_n - x_p \mp \Delta/2}{\gamma/2} \right) \right] \quad (64)$$

and $I_n = |A_p|^2 - I_{n-1} - I_{n+1}$, where $x_p = \alpha(p - \chi)\Omega + \bar{x}$. Letting $I_n \triangleq |A_p|^2 i_{p,n}$, for a single FSR we have

$$I_j = |A_{-1}|^2 (i_{-1,l-1} \delta_{j,l-1} + i_{-1,l} \delta_{j,l} + i_{-1,l+1} \delta_{j,l+1}) + |A_0|^2 (i_{0,m-1} \delta_{j,m-1} + i_{0,m} \delta_{j,m} + i_{0,m+1} \delta_{j,m+1}) + |A_{+1}|^2 (i_{+1,n-1} \delta_{j,n-1} + i_{+1,n} \delta_{j,n} + i_{+1,n+1} \delta_{j,n+1})$$

where l, m, n denote the indices of the central pixel for the $p = -1, 0, 1$ order peak respectively. An element of the FIM then follows as

$$[\mathbb{J}]_{i,k} = \frac{1}{\sigma^2} \frac{\partial^2}{\partial w_i \partial w_k} \sum_{p=-1}^1 |A_p|^4 i_{p,t(p)}^2 \quad (65)$$

where we have used the equivalent definition of FIM given in Eq. (22). It is important to note that in Eq. (65) we have introduced the mapping function $t(p)$. In particular $t(p)$ is the integer satisfying the inequality

$$x_t - \Delta/2 < \alpha(p - \chi)\Omega + \bar{x} \leq x_t + \Delta/2. \quad (66)$$

To gain further insight we temporarily re-define the pixel index j such that the j th

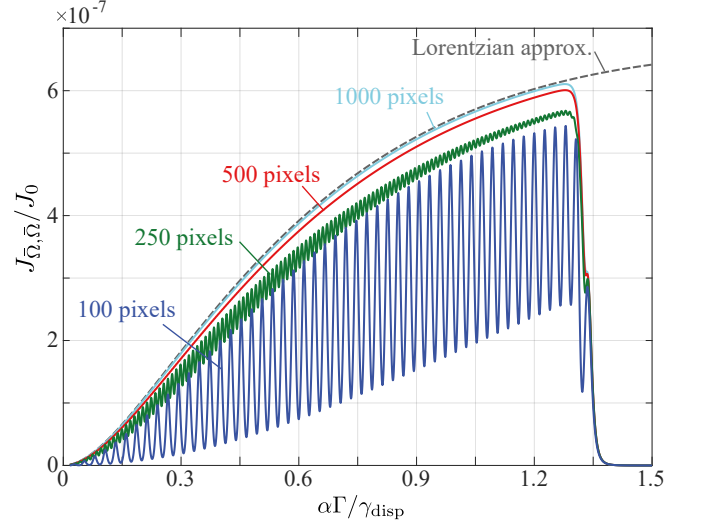


FIG. 6. Calculated Fisher information in the coarse pixellation limit. Peak widths of $\gamma_{\text{disp}} = 84 \mu\text{m}$ and $\gamma_{\text{opt}} = 8.4 \mu\text{m}$ were assumed, whilst the number of pixels on a finite size detector was varied. Other simulation parameters are given in Table I.

pixel is centred at $x = 0$, whereby $t = -\text{floor}[X/(2\Delta)], \dots, -1, 0, 1, \dots, \text{ceil}[X/(2\Delta)]$. Hence $x_t = t\Delta$ and t is the integer satisfying $t\Delta - \Delta/2 < x_p \leq t\Delta + \Delta/2$. Thus $x_p/\Delta - 1/2 \leq t < x_p/\Delta + 1/2$ implying

$$t = \text{round} \left[\frac{x_p}{\Delta} - \frac{1}{2} \right] = \text{round} \left[\frac{\alpha(p - \chi)\Omega}{\Delta} + \frac{\bar{x}}{\Delta} - \frac{1}{2} \right]. \quad (67)$$

Typically $\Omega/\Delta \gg 1$ implying that t , and hence the acquired FIM, oscillates rapidly as a function of α . Since α describes the linear mapping between the frequency and spatial domain, this means that the obtainable FIM, and hence the obtainable precision, is strongly dependent on the angular dispersion of the spectrometer and the optical magnification in the coarse pixellation regime. This behaviour is to be expected because in this regime the details of the spectral peak are barely resolvable by the detector. Similarly, the obtainable precision depends strongly on the registration of the incident spectrum with respect to the detector pixels, as parametrised by \bar{x} . To illustrate the oscillations we have numerically calculated $J_{\bar{\Omega}, \bar{\Omega}}$ for a detector with varying numbers of pixels. Specifically we use the parameters given in Table I and consider a detector with 100, 250, 500 and 1000 pixels (corresponding to pixel sizes of 140, 56, 28, 14 μm respectively). The width of the dispersive element's response function was fixed at $\gamma_{\text{disp}} = 84 \mu\text{m}$, whilst the numerical aperture of the relay lens was set such that $\gamma_{\text{opt}} = \gamma_{\text{disp}}/10$. With these parameters the simulated spectrometer operates within the dispersion limited regime. Numerical results are shown in Figure 6. For the largest pixel size (corresponding to $\gamma_{\text{disp}} = 0.6$

pixels) large oscillations in $J_{\bar{\Omega},\bar{\Omega}}$ are observed. The magnitude of these oscillations decrease as the pixel size increases until the finely pixellated regime is reached. We note that in these simulations the larger choice of γ_{disp} means that the optimal configuration ($\rho = 2$) requires a scaling factor α for which the inelastic spectral peaks lie beyond the detector and no information regarding Ω can be obtained. In turn this means that the peak in $J_{\bar{\Omega},\bar{\Omega}}$ is not seen (as compared to e.g. Figure 2). Instead the optimal α is that for which the inelastic peaks lie just within the spatial extent of the detector (assuming that the Rayleigh peak is centred).

CONCLUSIONS

In this paper we have established the fundamental precision limits achievable when determining key spectral parameters in inelastic optical spectroscopy. In such applications, parameters such as the frequency shift of Raman or Brillouin scattered photons and the linewidth of the corresponding spectral peaks are of interest since they can provide quantitative information about the micro-mechanical, elastic and molecular information of material samples. Precision limits were derived using the concept of Fisher information and the Cramér-Rao lower bound and took account of the instrument response function of the dispersive element and potential defocus or spherical aberration in the detection optics, in addition to the size and pixellation of the detector itself. As such our

results are applicable to a broad range of spectroscopic instruments. We also note that such limits are asymptotically achievable through use of a maximum likelihood estimation strategy.

Although general formulae were given, a number of limiting cases were also considered providing greater insight into the obtainable precision. Specifically, we gave simplified results for both a dispersion and diffraction limited spectrometer. Optimal configurations (in terms of angular dispersion or optical magnification) could then be found for estimation of either the central frequency, inelastic shift or peak width. These optima occur when the competing effects of the experimental lineshape and spatial separation of peaks on the detector are balanced. Numerical calculations were also presented for more general scenarios. For fixed dispersion/magnification the obtainable precision was thereby found to worsen as the widths of the response functions increased. Defocus and spherical aberration in the relay optics were also found to reduce the obtainable precision as would be intuitively expected, however, their effect on determining the optimal spectrometer configurations was found to be minimal even for relatively strong aberration strengths. Finally, although detector pixellation was shown to imply that informational limits can be highly sensitive to detector registration and other experimental parameters, this was only found to be significant in the coarse pixellation regime whereby spectral linewidths and pixel size are comparable. Given the high pixel count on many modern day detectors, this is unlikely to be of practical importance.

-
- [1] Leon Brillouin, "Diffusion of light and x-rays by a transparent homogeneous body," *Ann. Phys* **17**, 88–122 (1922).
 - [2] C V Raman, "A New Radiation," *Indian J. Phys.* **2**, 387–398 (1927).
 - [3] Ewen Smith and Geoffrey Dent, *Modern Raman spectroscopy - a practical approach* (John Wiley & Sons, Ltd, Chichester, UK, 2005).
 - [4] A K M S Chowdhury, D C Cameron, and J Hashmi, "Vibrational properties of carbon nitride films by Raman spectroscopy," *Thin Solid Films* **332**, 62–68 (1998).
 - [5] Kristie J Koski, Paul Akhenblit, Keri Mckiernan, and Jeffery L Yarger, "Non-invasive determination of the complete elastic moduli of spider silks," *Nat. Materials* **12**, 262–267 (2013).
 - [6] Shaoliang Sheng, Jiang-Bin Wu, Xin Cong, Wenbin Li, Jian Gou, Qing Zhong, Peng Cheng, Ping-Heng Tan, Lan Chen, and Kehui Wu, "Vibrational Properties of a Monolayer Silicene Sheet Studied by Tip-Enhanced Raman Spectroscopy," *Phys. Rev. Lett.* **119**, 196803 (2017).
 - [7] Pei Jung Wu, Irina V. Kabakova, Jeffrey W. Ruberti, Joseph M. Sherwood, Iain E. Dunlop, Carl Paterson, Peter Török, and Darryl R. Overby, "Water content, not stiffness, dominates Brillouin spectroscopy measurements in hydrated materials," *Nat. Methods* **15**, 561–562 (2018).
 - [8] Irina V. Kabakova, YuChen Xiang, Carl Paterson, and Peter Török, "Fiber-integrated Brillouin microspectroscopy: Towards Brillouin endoscopy," *J. Innov. Opt. Health. Sci.* **10**, 1742002 (2017).
 - [9] Cristina L Zavaleta, Ellis Garai, Jonathan T C Liu, Steven Sensarn, Michael J Mandella, Dominique Van De Sompel, Shai Friedland, Jacques Van Dam, Christopher H Contag, Sanjiv S Gambhir, and Michael E Phelps, "A Raman-based endoscopic strategy for multiplexed molecular imaging," *Proc. Natl. Acad. Sci. USA* **110**, E2288–E2297 (2013).
 - [10] K. J. Koski and J. L. Yarger, "Brillouin imaging," *Appl. Phys. Lett.* **87**, 1–4 (2005).
 - [11] Giuliano Scarcelli and Seok Hyun Yun, "Confocal Brillouin microscopy for three-dimensional mechanical imaging," *Nat. Photon.* **2**, 39–43 (2008).
 - [12] C. L. Jahncke, M. A. Paesler, and H. D. Hallen, "Raman imaging with nearfield scanning optical microscopy," *Appl. Phys. Lett.* **67**, 2483–2485 (1995).
 - [13] Jens Steidtner and Bruno Pettinger, "Tip-Enhanced Raman Spectroscopy and Microscopy on Single Dye Molecules with 15 nm Resolution," *Phys. Rev. Lett.* **100**, 236101 (2008).
 - [14] Peter Vohringer and Norbert F Scherer, "Transient Grating Optical Heterodyne Detected Impulsive Stimulated Raman Scattering in Simple Liquids," *J. Phys. Chem.*

- [99](#), 2684–2695 (1995).
- [15] Sebastian Schlücker, ed., *Surface Enhanced Raman Spectroscopy: Analytical, Biophysical and Life Science Applications* (Weinheim, Germany, 2011).
- [16] Charles W Ballmann, Zhaokai Meng, Andrew J Traverso, Marlan O Scully, and Vladislav V Yakovlev, “Impulsive Brillouin microscopy,” *Optica* **4**, 124–128 (2017).
- [17] Hajime Tanaka and Tsuyoshi Sonehara, “New Method of Superheterodyne Light Beating Spectroscopy for Brillouin Scattering Using Frequency-Tunable Lasers,” *Phys. Rev. Lett.* **74**, 1609–1612 (1995).
- [18] Giuseppe Antonacci, Guillaume Lepert, Carl Paterson, and Peter Török, “Elastic suppression in Brillouin imaging by destructive interference,” *Appl. Phys. Lett.* **107**, 061102 (2015).
- [19] Bryan T Bowie, D Bruce Chase, and Peter R Griffiths, “Factors affecting the Performance of Bench-Top Spectrometers. Part I : Instrumental Effects,” *Appl. Spectrosc.* **54**, 164A–173A (2000).
- [20] Giuseppe Antonacci, Matthew R Foreman, Carl Paterson, and Peter Török, “Spectral broadening in Brillouin imaging,” *Appl. Phys. Lett.* **103**, 221105 (2013).
- [21] Zachary Coker, Maria Troyanova-wood, Andrew J Traverso, Talgat Yakupov, Zhandos N Utegulov, and Vladislav V Yakovlev, “Assessing performance of modern Brillouin spectrometers,” *Opt. Express* **26**, 2400–2409 (2018).
- [22] C Craggs, K P Galloway, and D J Gardiner, “Maximum entropy methods applied to simulated and observed Raman spectra,” *Appl. Spectrosc.* **50**, 43–47 (1996).
- [23] YuChen Xiang, Matthew R Foreman, and Peter Török, “SNR Enhancement in Brillouin Microspectroscopy using Spectrum Reconstruction,” in preparation (2018).
- [24] P A Wilksch, “Instrument function of the Fabry-Perot spectrometer,” *Appl. Opt.* **24**, 1502–1511 (1985).
- [25] Shijun Xiao, Andrew M Weiner, and Christopher Lin, “A dispersion law for virtually imaged phased-array spectral dispersers based on paraxial wave theory,” *IEEE J. Quantum Elect.* **40**, 420–426 (2004).
- [26] Masataka Shirasaki, “Virtually Imaged Phased Array,” *Fujitsu Sci. Tech. J.* **35**, 113–125 (1999).
- [27] Max Born and Emil Wolf, *Principles of Optics*, 6th ed. (1980).
- [28] Joseph W Goodman, *Introduction to Fourier Optics*, 2nd ed. (McGraw Hill, 1996).
- [29] Richard Barakat and Leslie Riseberg, “Diffraction Theory of the Aberrations of a Slit Aperture,” *J. Opt. Soc. Am.* **55**, 878–881 (1965).
- [30] Louis L Scharf, *Statistical Signal Processing - Detection, Estimation, and Time Series Analysis* (Addison-Wesley Publishing Co., USA, 1991).
- [31] Matthew R Foreman and Peter Török, “Information and resolution in electromagnetic optical systems,” *Phys. Rev. A* **82**, 043835 (2010).
- [32] A. Zeira and A. Nehorai, “Frequency domain Cramer-Rao bound for Gaussian processes,” *IEEE T. Acoust. Speech.* **38**, 1063–1066 (1990).
- [33] Matthew R Foreman, Wei-Liang Jin, and Frank Vollmer, “Optimizing detection limits in whispering gallery mode biosensing,” *Opt. Express* **22**, 5491–5511 (2014).
- [34] T. Ida, M. Ando, and H. Toraya, “Extended pseudo-Voigt function for approximating the Voigt profile,” *J. Appl. Crystal.* **33**, 1311–1316 (2000).